Supporting Information

Mg-Vacancies Induced Ni-Vacancy Clusters: Highly Efficient Hydrogen Production from Cellulose

Jian Zhang,[1] Yanru Zhu, [1] Zhe An, [1] Xin Shu, [1] Xiaodan Ma, [1] Hongyan Song, [1] Wenlong Wang, [1] Jieqiong Zhao,[1] Xingzhong Cao, [2] and Jing He [1]**

[1] State Key Laboratory of Chemical Resource Engineering & Beijing Advanced Innovation Center for Soft Matter Science and Engineering, Beijing University of Chemical Technology, Beijing 100029, China

[2] Multi-discipline Research Division, Institute of High Energy Physics, Chinese Academy of Sciences, Beijing 100049, China

*corresponding author. Tel: +86-010-88233393. E-mail address: caoxzh@ihep.ac.cn;

*corresponding author. Tel: +86-10-64425280. Fax: +86-10-64425385. E-mail address: jinghe@263.net.cn or hejing@mail.buct.edu.cn. Postal address: Box 98, 15 Beisanhuan Donglu, Beijing 100029, China

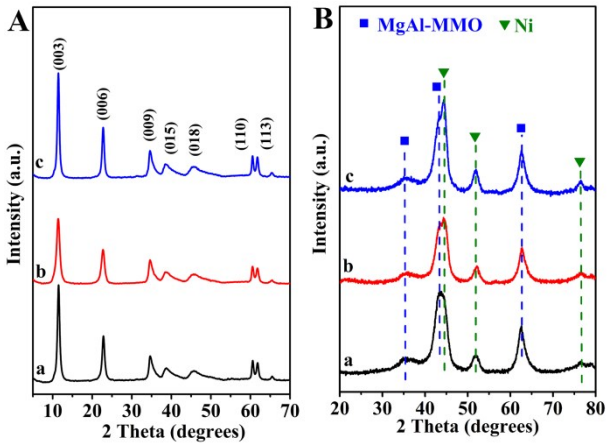

Figure S1. XRD patterns of (A) as-prepared and (B) calcined (in H_2 flow) (a) Ni-MgAl-LDHs-G, (b) Ni-MgAl-LDHs-C, and (c) Ni-MgAl-LDHs-G-Mg.

The (003), (006), (012), (015), (018), (110), and (113) reflections typical of LDH structure are clearly observed (**Figure S1, A**). In each case, no other phases are observed (**Figure S1, A**). After calculation under H_2 atmosphere, the reflections characteristic of metallic Ni and Mg-Al mixed metal oxide (MgAl-MMO) phases are observed (**Figure S1, B**).

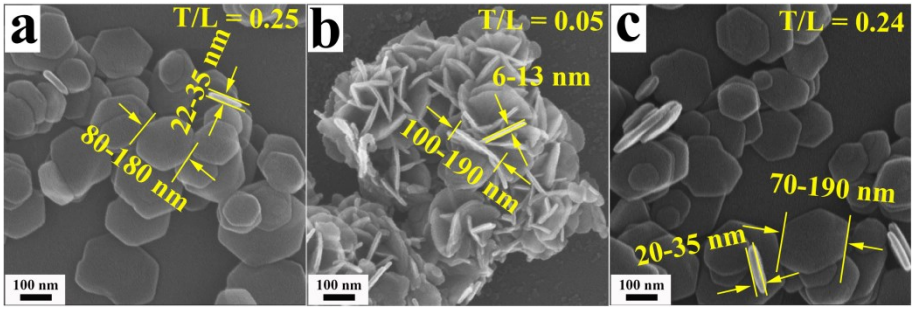

Figure S2. SEM images of (a) Ni-MgAl-LDHs-G, (b) Ni-MgAl-LDHs-C, and (c) Ni-MgAl-LDHs-G-Mg.

Ni-MgAl-LDHs-G is composed of individual sheets with 80-180 nm in length and 22-35 nm in thickness while Ni-MgAl-LDHs-C is composed of numerous frizzy nanoflakes with 100-190 nm in length and 6-13 nm in thickness. Re-aging Ni-MgAl-LDHs-G in the solution of $Mg(NO_3)_2$ retains the morphology of the pristine LDHs.

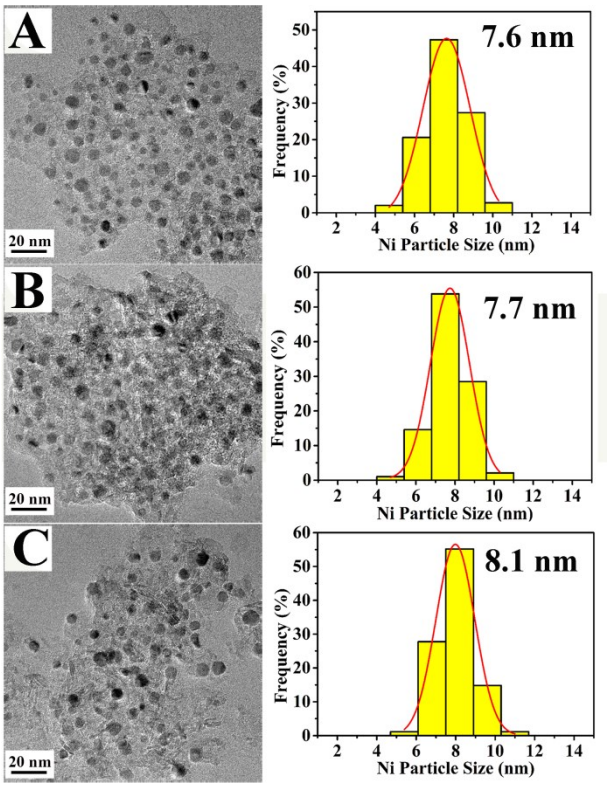

Figure S3. TEM images and size distribution of metallic Ni particles prepared by calcination under H_2 atmosphere of (A) Ni-MgAl-LDHs-G, (B) Ni-MgAl-LDHs-C, and (C) Ni-MgAl-LDHs-G-Mg.

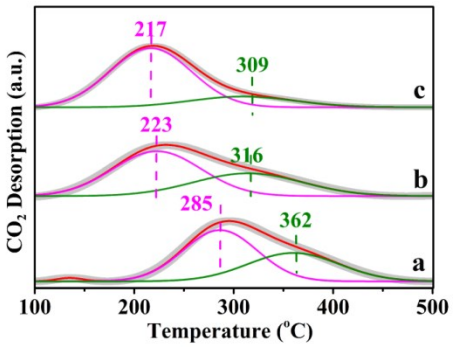

Figure S4. CO_2-TPD profiles deconvoluted into peaks corresponding to medium-strong base (II, magenta) and strong base (III, green) site for (a) Ni-MgAl-MMO-G, (b) Ni-MgAl-MMO-C, and (c) Ni-MgAl-MMO-G-Mg.

For each sample, the CO_2-TPD profiles can be deconvoluted into two or three peaks corresponding to weak base (I, blue), medium-strong base (II, magenta) and strong base (III, green) sites. The total amount of medium-strong and strong basic sites is summarized in **Table S1**.

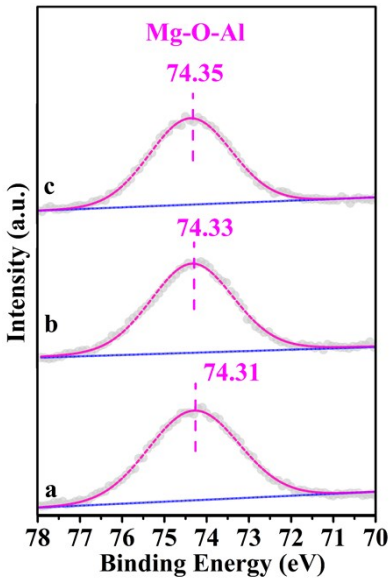

Figure S5. Quasi in-situ XPS spectra of Al 2p for (a) Ni-MgAl-MMO-G, (b) Ni-MgAl-MMO-C, and (c) Ni-MgAl-MMO-G-Mg. No obvious difference in Al 2p binding energy is detected.

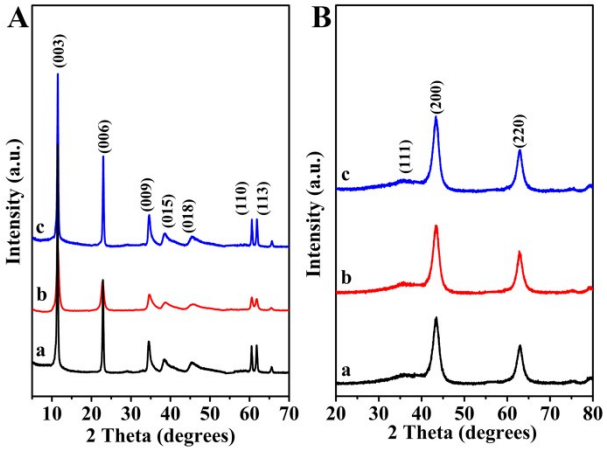

Figure S6. XRD patterns of (A) as-prepared and (B) calcined (in H_2 flow) (a) MgAl-LDHs-G, (b) MgAl-LDHs-C, and (c) MgAl-LDHs-G-Mg.

The (003), (006), (012), (015), (018), (110), and (113) reflections typical of LDH structure are clearly observed (**Figure S6, A**). In each case, no other phases are observed (**Figure S6, A**).

After calculation under H_2 atmosphere, the reflections characteristic of MgAl-MMO phases are observed (**Figure S6, B**).

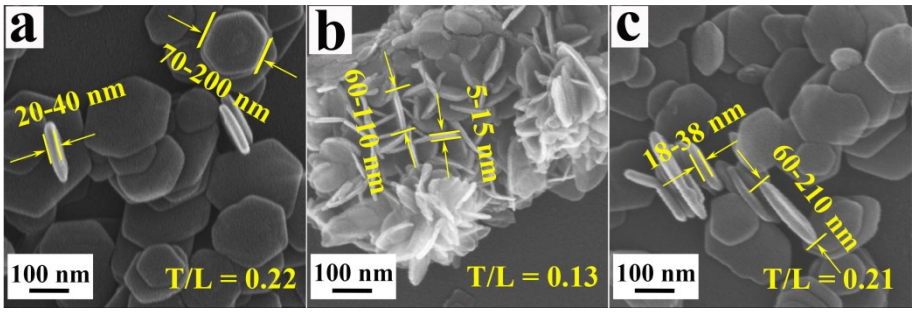

Figure S7. SEM images of (a) MgAl-LDHs-G, (b) MgAl-LDHs-C, and (c) MgAl-LDHs-G-Mg. Similar morphology to its counterpart Ni-MgAl-LDHs is obtained for either MgAl-LDHs-G or MgAl-LDHs-C. No changes in the morphology are clearly observed after re-aging MgAl-LDHs-G in the solution of $Mg(NO_3)_2$.

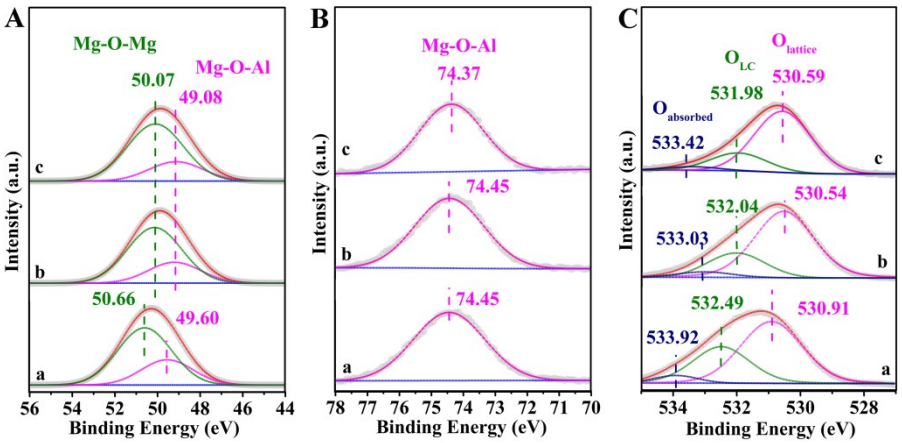

Figure S8. Quasi in-situ XPS spectra for (A) Mg 2p, (B) Al 2p, and (C) O 1s of (a) MgAl-MMO-G, (b) MgAl-MMO-C, and (c) MgAl-MMO-G-Mg.

The Mg 2p binding energy (**Figure S8, A**) on MgAl-MMO-G is 0.52~0.59 eV higher than that on MgAl-MMO-C, indicative of more electron-deficiency of the Mg (II) sites in MgAl-MMO-G. Besides, the surface Mg/Al molar ratio for MgAl-MMO-G determined by XPS was 2.39/1.00 (**Table S2**) while 2.85/1.00 for MgAl-MMO-C (**Table S2**), indicative of the presence of Mg vacancies (V_{Mg}) on the surface of MgAl-LDHs-G. Also, the ratio of surface Mg-O-Mg to Mg-O-Al (**Table S2**) on MgAl-MMO-G, calculated by the corresponding deconvoluted XPS area, is only 2.37, lower than that on MgAl-MMO-C (2.80), demonstrating the loss of Mg (II) sites in Mg-O-Mg linkage on MgAl-MMO-G. Almost no difference in Al 2p binding energy is obviously observed (**Figure S8, B**), further confirming the loss of Mg (II) sites in Mg-O-Mg rather than Mg-O-Al. In the O 1s XPS spectra (**Figure S8,**

C), higher O_{LC} concentration is clearly observed on MgAl-MMO-G than on MgAl-MMO-C (**Table S2**). The XPS results clearly display MgAl-MMO-G has more V_{Mg} sites than MgAl-MMO-C.

The binding energy of Mg 2p (**Figure S8, A**) and O 1s (**Figure S8, C**) for MgAl-MMO-G-Mg decrease in comparison to that for MgAl-MMO-G, approaching the value observed for MgAl-MMO-C, indicative of the elimination of V_{Mg} sites on MgAl-MMO-G-Mg. Similar Al 2p binding energy (**Figure S8, B**) is observed on MgAl-MMO-G-Mg to on MgAl-MMO-G.

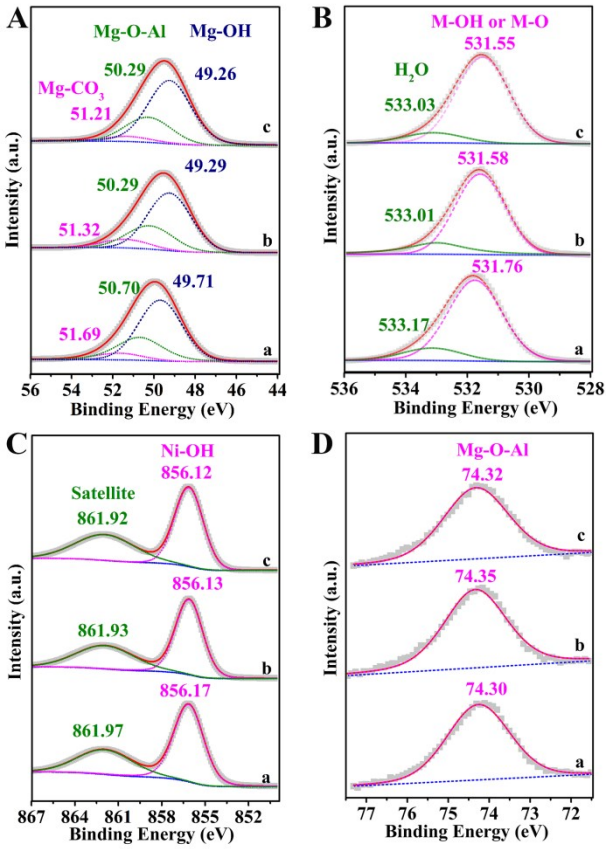

Figure S9. XPS spectra for (A) Mg 2p, (B) O 1s, (C) Ni $2p_{3/2}$, and (D) Al 2p of (a) Ni-MgAl-LDHs-G, (b) Ni-MgAl-LDHs-C, and (c) Ni-MgAl-LDHs-G-Mg.

Three Mg 2p peaks attributed to Mg-OH, Mg-O-Al, and $MgCO_3$ are observed (**Figure S9, A**). The binding energy of Mg 2p for Ni-MgAl-LDHs-G is observed almost 0.5 eV higher than that for Ni-MgAl-LDHs-C, indicating the electron-deficiency of Mg in the Ni-MgAl-LDHs-G. Two O 1s binding energies assigned to M-OH or M-O at 531.55-531.76 eV and H_2O at 533.01-533.17 eV are detected in the O 1s spectra (**Figure S9, B**). Also, the O 1s binding energy for Ni-MgAl-LDHs-G is 0.18 eV higher than that for Ni-MgAl-LDHs-C, indicative of the electron-deficient O for Ni-MgAl-LDHs-G. But almost no obvious difference in the binding energies of Ni $2p_{3/2}$ or

Al 2p is observed between Ni-MgAl-LDHs-G and Ni-MgAl-LDHs-C (**Figure S9, C** and **D**).

The binding energy of either Mg 2p (**Figure S9, A**) or O 1s (**Figure S9, B**) for Ni-MgAl-LDHs-G-Mg decreases in comparison to Ni-MgAl-LDHs-G, to the same level as that for Ni-MgAl-LDHs-C. The binding energy of either Ni 2p (**Figure S9, C**) or Al 2p (**Figure S9, D**) hardly changes in the re-aging. That indicates that re-aging in solution of $Mg(NO_3)_2$ clearly eliminates the V_{Mg} sites on Ni-MgAl-LDHs-G.

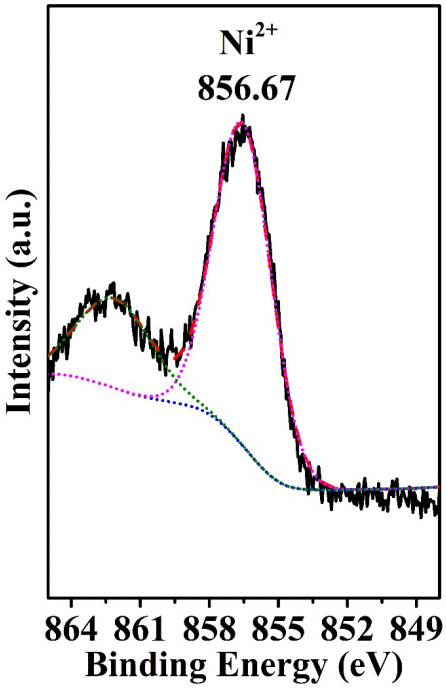

Figure S10. XPS spectrum of NiMgAl-MMO-C prepared by thermal treatment of Ni-MgAl-LDHs-C under N_2 at 800 ^oC.

The binding energy for Ni^{2+} species is observed at 856.67 eV in the NiMgAl-MMO-C prepared by thermal treatment of Ni-MgAl-LDHs-C under N_2 at 800 ^oC.

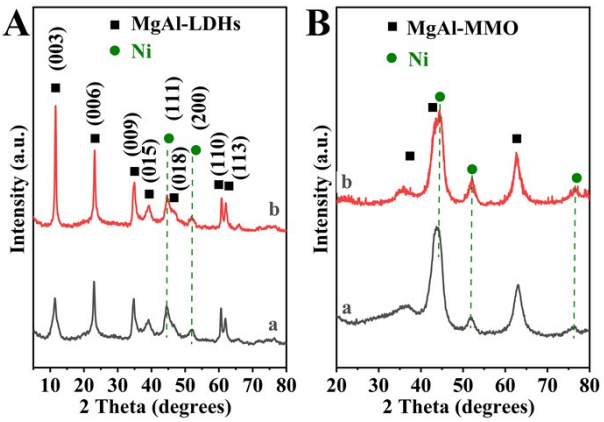

Figure S11. XRD patterns of (A) spent and (B) regenerated (a) Ni-MgAl-MMO-G and (b) Ni-MgAl-MMO-C.

During the APR process, the restoration of MgAl-MMO to MgAl-LDHs occurs while the metallic Ni is still observed. Almost no changes in the half width of Ni (200) at 51.8° are detected compared to the fresh counterparts, demonstrating that no aggregation of Ni particles occurs. After regeneration by calcination and followed reduction, similar XRD patterns to the fresh counterparts are observed.

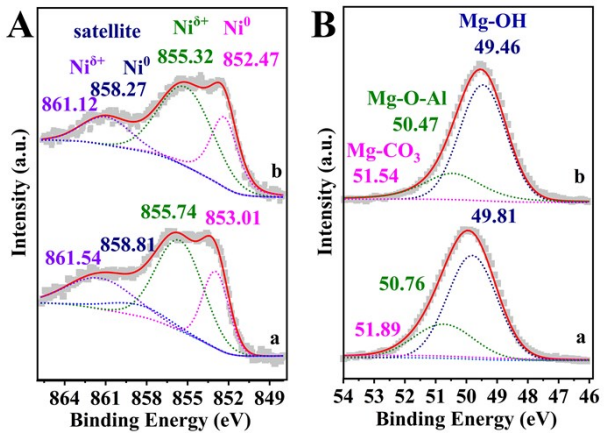

Figure S12. XPS spectra for (A) Ni $2p_{3/2}$ and (B) Mg 2p of spent (a) Ni-MgAl-MMO-G and (b) Ni-MgAl-MMO-C.

After the APR process, almost no change in the binding energy of Ni^0 is detected on spent Ni-MgAl-MMO compared to the fresh counterparts. The binding energy of $Ni^{\delta+}$ slightly lowers from 856.08 eV (855.58 eV) to 855.74 eV (855.32 eV) with the population of $Ni^{\delta+}$ sites decreasing from 82 % (81 %) to 68 % (65 %) on spent Ni-MgAl-MMO. The Mg 2p binding energies of Mg-OH, Mg-O-Al, and $MgCO_3$ are detected due to the restoration of MgAl-MMO to MgAl-LDHs. The Ni $2p_{3/2}$ binding energies assigned to Ni^0 and $Ni^{\delta+}$ or Mg 2p binding energies of Mg-OH, Mg-O-Al, and $MgCO_3$ for spent Ni-MgAl-MMO-G are observed higher than that for spent Ni-MgAl-MMO-C. And the surface Ni/Mg/Al molar ratio determined by XPS was 0.78/2.53/1.00 (**Table S2**) for spent Ni-MgAl-MMO-G while 0.79/2.81/1.00 for spent Ni-MgAl-MMO-C (**Table S2**). These results are similar to the fresh

counterparts, indicating that spent Ni-MgAl-MMO has been well regenerated and the V_{Mg} and Ni vacancies or Ni vacancy cluster on the spent Ni-MgAl-MMO-G has been well retained.

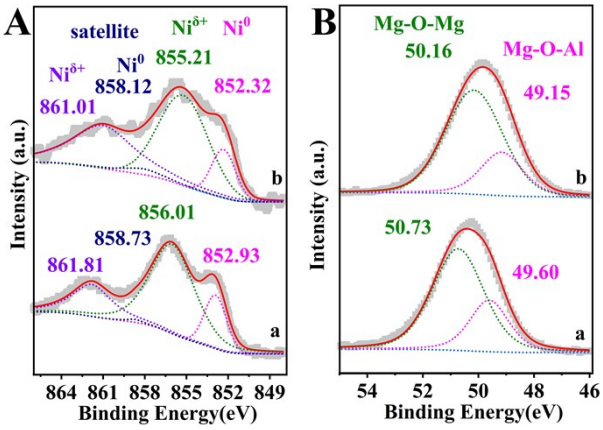

Figure S13. XPS spectra for (A) Ni $2p_{3/2}$ and (B) Mg 2p of regenerated (a) Ni-MgAl-MMO-G and (b) Ni-MgAl-MMO-C.

After regeneration, similar XPS results to the fresh counterparts are observed.

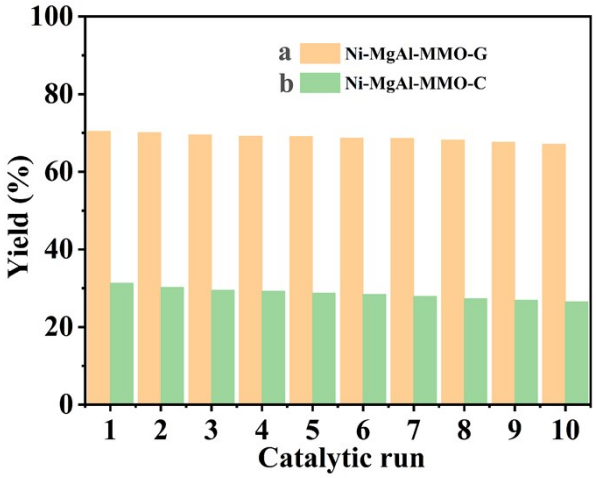

Figure S14. Variation of H_2 production versus catalytic run of (a) Ni-MgAl-MMO-G and (b) Ni-MgAl-MMO-C.

H_2 yield only decreases by 4.7 % (from 70.4 % to 67.1 %) on Ni-MgAl-MMO-G in tenth run, while decreases by 15.3 % (from 31.3 % to 26.5 %) on Ni-MgAl-MMO-C, displaying well reusability of Ni-MgAl-MMO-G.

Table S1. Chemical, physical, and acid-base properties of Ni-NiAl-LDO.

Samples	Ni/Mg/Al ratio by ICP	BET surface area (m^2/g)	Ni particle size (nm)	Ni dispersity (%)	Basic sites (mmol CO_2/g)		B_S/B_M
					B_M	B_S	
Ni-MgAl-MMO-G	0.81/3.0/1.0	220	7.6	12.3	0.49	0.33	0.67
Ni-MgAl-MMO-C	0.81/3.0/1.0	215	7.7	12.1	0.63	0.22	0.35
Ni-MgAl-MMO-G-Mg	0.81/3.1/1.0	216	8.1	11.5	0.71	0.16	0.23
MgAl-MMO-G	0/3.0/1.0	240	-	-	N.D.	N.D.	N.D.
MgAl-MMO-C	0/3.0/1.0	237	-	-	N.D.	N.D.	N.D.
MgAl-MMO-G-Mg	0/3.1/1.0	223	-	-	N.D.	N.D.	N.D.

Table S2. XPS results of MgAl-MMO with or without Ni particles.

Samples	Ni/Mg/Al ratio	Mg-O-Mg/Mg-O-Al	O_{LC}/%	$Ni^{\delta+}$/%
Ni-MgAl-MMO-G	0.79/2.41/1.00	2.37	33.3	82
Ni-MgAl-MMO-C	0.80/2.83/1.00	2.78	23.2	81
Ni-MgAl-MMO-G-Mg	0.81/2.91/1.00	3.08	20.5	81
Ni-MgAl-LDHs-G	0.79/2.51/1.00	-	-	-
Ni-MgAl-LDHs-C	0.80/2.72/1.00	-	-	-
Ni-MgAl-LDHs-G-Mg	0.80/2.81/1.00	-	-	-
MgAl-MMO-G	2.39/1.00	2.37	34.4	-
MgAl-MMO-C	2.85/1.00	2.80	23.3	-
MgAl-MMO-G-Mg	2.93/1.00	3.04	21.5	-
Spent Ni-MgAl-MMO-G	0.78/2.53/1.00	-	-	68
Spent Ni-MgAl-MMO-C	0.79/2.81/1.00	-	-	65
Regenerated Ni-MgAl-MMO-G	0.80/2.47/1.00	2.44	-	79
Regenerated Ni-MgAl-MMO-C	0.79/2.89/1.00	2.87	-	80